Shap. Mem. Superelasticity (2020) 6:342–353
https://doi.org/10.1007/s40830-020-00298-8

SPECIAL ISSUE: A TRIBUTE TO PROF. DR. GUNTHER EGGELER, INVITED PAPER

Selective Laser Melting of NiTi Shape Memory Alloy: Processability, Microstructure, and Superelasticity

Carlo Alberto Biffi[1] · Jacopo Fiocchi[1] · Fabrizio Valenza[2] · Paola Bassani[1] · Ausonio Tuissi[1]

Published online: 3 August 2020

Abstract Nowadays, thanks to the growing interest regarding the manufacturing of 3D complex parts with integrated functionalities, the additive manufacturing of NiTi shape memory alloy is a challenging technological issue. Particularly, 3D printing of NiTi components requires a strong interaction between technological and metallurgical approaches, due to the significant correlation among the process conditions, the microstructure, and the functional performances. The goals of the present work are to define the processability of NiTi powder for realizing fully dense samples using Selective Laser Melting process and the correlation between the microstructure and the superelastic response of specimens processed in different process conditions. It was found that highest relative density values can be obtained for a laser fluence in the range 63–160 J/mm^3. The resulting microstructures exhibit variable degrees of orientations, according to the different cooling rates and melt pool size, specific for each condition. Finally, mechanical testing in compression indicated that the as-built alloy exhibits a limited superelastic behavior. A typical flag-like behavior, characterized by 6% of complete recoverable strain, was obtained through heat treatment at 500 °C. This suggests that the microstructure of as-built samples is highly efficient to promote superelasticity after annealing.

Keywords NiTi · Shape memory alloy · Selective laser melting · Microstructure · EBSD · Martensitic transformation · Superelasticity

✉ Ausonio Tuissi
ausonio.tuissi@cnr.it

Carlo Alberto Biffi
carloalberto.biffi@cnr.it

[1] National Research Council of Italy - Institute of Condensed Matter Chemistry and Technologies for Energy, Unit of Lecco, CNR ICMATE, Via Previati 1/E, 23900 Lecco, Italy

[2] National Research Council of Italy - Institute of Condensed Matter Chemistry and Technologies for Energy, Unit of Genova, CNR ICMATE, Via de Marini, 6, 16149 Genova, Italy

Introduction

Shape Memory Alloys (SMAs) are functional materials, which are well known for their unique properties, namely, shape memory effect (SME) and pseudoelasticity (PE) [1]. Due to its stable and optimal properties, intermetallic NiTi compound is the most widespread SMA. These peculiar characteristics are due to a diffusionless solid-to-solid phase transformation, namely, martensitic transformation (MT), which can be found in Ti-rich NiTi and Ni-rich NiTi alloys above or below room temperature, respectively. The temperature range, at which the MT occurs, dictates the use of these materials as actuators or for biomedical devices showing SME or PE, respectively. However, the use of Ni-rich NiTi alloy, showing SE at room temperature, was also demonstrated to be suitable for developing high-performance actuators based on heating and cooling of the stress-induced martensite [2]. Transformation temperatures of the MT are strongly affected by Ni/Ti ratio, and stable functional characteristics are obtained through challenging processes [3, 4]. The limited processability of NiTi through conventional manufacturing methods [5, 6] stimulates the use of advanced manufacturing processes [7], like laser welding [8–11] and cutting [12], and additive manufacturing (AM) [13, 14]. The formers are the most adopted in industrial applications, while the latter is nowadays widely experimented in scientific fields. Due to the benefits of AM

[15, 16], such as the realization of complex parts and the possible redesign of the components according with the concept of placing material only where it is necessary, NiTi can be considered as one of the most promising alloys produced by AM, only superseded by industrially recognized metallic powders. On the other side, there are significant issues to be taken into account, including Ni loss [17], appropriate heat treatments [18], and optimization of functional performances of the parts [19].

The manufacturing of NiTi SMAs using different AM technologies, such as Powder Bed processes (Selective Laser Melting—SLM and Electron Beam Melting—EBM) and Direct Energy Deposition (DED), has been deeply studied in several experimental works [13, 20–22]. Among these AM methods, nowadays, the SLM process appears to be the best solution for nearly equiatomic NiTi compound. In fact, SLM can be considered the most proper one not only due to its reasonable ability of protecting both powder and liquid pool from oxidation, but also for its capability of limiting the Ni evaporation, counteracted by the pressure of the inert gas present in the chamber. Several works focusing on the microstructure and functional properties of SLM-built samples, manufactured using Ni-rich NiTi, can be found in the literature, specifically for biomedical applications [19]. It was found that MT temperatures comparable to those of the wrought alloy can be obtained [23, 24], even though the strict control of the Ni/Ti ratio is a challenging issue [25, 26]. Another relevant difference between SLMed and wrought NiTi lies in the different texture orientations, which arises from the manufacturing characteristics, such as cooling rates and thermal gradients. In fact, the SLMed microstructure can be strongly textured, depending of the process conditions [27], and this feature may be optimized for tailoring the functional performances of the NiTi parts [23, 24, 28–31].

However, all the mentioned works are related to the SLM process carried out using a continuous wave (CW) laser emission mode. It is well known from laser material processing that the use of continuous wave (CW) and pulsed wave (PW) laser emission modes can promote modifications in the processability map and in the microstructure of metals [32–34]. The literature reports several works regarding the use of CW laser emission mode in SLM of NiTi alloys, while no available information on the use of PW lasers for printing NiTi alloys can be found in the literature.

Therefore, the scope of the present work is to identify the technological window for realizing fully dense samples using the PW laser emission mode and to correlate different process conditions to the microstructure and the functional properties of NiTi SLMed specimens.

It was found that the relative density maximum is associated to a laser fluence range, which is able to promote microstructures exhibiting different levels of orientations, according to variable cooling rates and different melt pool sizes. The induced fluence can also induce a shift of the martensitic transformation temperatures to higher values, accordingly, with the use of higher laser pulse energies. Finally, mechanical testing in compression indicated that the as-built alloy exhibits a limited superelastic behavior; on the contrary, a typical flag-like behavior, characterized by 6% of complete recoverable strain, was obtained after a heat treatment at 500 °C.

Experimental

Selective Laser Melting Process

Cylindrical samples (3 mm in diameter, 5 mm in height) were produced from Ni50.8Ti49.2 (at%) spherical powder by means of a SLM system (mod. AM400 from Renishaw) equipped with a pulsed wave laser with a maximum power of 400 W. The process parameters, listed in Table 1, were used for manufacturing cylinders printed on a Ti6Al4V platform at room temperature [31]. Full factorial design was performed for fixing the optimal set of process parameters able to maximize the relative density.

Sample Characterizations

Density measurements were performed with a Gibertini E 50 S/2 balance equipped with a set up for implementing the Archimedes method on all the SLMed samples. Relative density is evaluated by ratio between the measured density and the nominal density of 6.45 g/cm^3. This procedure was carried out in order to define the process conditions able to guarantee the highest values of relative density in function of the laser power density per unit of volume, namely, fluence, which was calculated as follows (Eq. 1):

Table 1 List of variable and fixed process parameters used for printing NiTi cylinders

Parameters	Values
Power	30-40-50-75-100-125-150-175 W
Exposition time	25-50-75-100-125-150 μs
Scanning strategy	Meander
Atmosphere	Argon
Layer thickness	30 μm
Hatch distance	50 μm
Point distance	50 μm
Laser spot size	65 μm
Oxygen level	< 20 ppm

$$F = \frac{P \cdot t_{exp}}{d_p \cdot d_h \cdot s} \quad (1)$$

where P, t_{exp}, d_p, d_h, and s indicate laser power, exposition time, point distance, hatch distance, and layer thickness, respectively [31].

Two process conditions, in correspondence of low and high fluence, were selected in the peak of the relative density of the samples in order to perform further analysis.

X-ray CT was performed on selected cylinders using a Phoenix v|tome|x M 300 CT system (Baker Hughes) having a tension of 300 kV and spatial resolution below 1 mm; the types of defects within the entire volume of the samples were analyzed.

Roughness of the upper surfaces of the built cylinders were quantitatively evaluated by using a 3D non-contact profilometer (Sensofar S-neox) equipped with an interferometric 10 × objective (vertical resolution: 1 nm; spatial sampling: 1.29 µm) and a confocal 100x (vertical resolution: 2 nm; spatial sampling: 0.13 µm) CF60-2 Nikon objectives. Quantitative measurements according to the ISO 25178 standard have been performed using the software embedded in the system (SensoSCAN).

Calorimetric properties of the SLMed NiTi samples were investigated through a differential scanning calorimeter (DSC, mod. SSC 5200 by Seiko Instruments), in the [− 100 °C; 150 °C] range with heating/cooling rate of 10 °C min; five complete thermal cycles were performed for each sample. Characteristic temperatures and corresponding transformation enthalpies were evaluated for both direct/reverse transformations upon cooling/heating, respectively.

Microstructure was investigated through Scanning Electron Microscopy (SEM), coupled with Electron Back Scatter Diffraction (EBSD) and energy Dispersive X-ray Spectroscopy (EDXS), on the xy and xz views for the three selected samples (FEG-SEM mod. SU70 from Hitachi, equipped with EBSD and EDXS systems from ThermoFisher Scientific). Sections were cut with a precision cut-off machine, and then included in graphite-loaded hot mounting resin, and after conventional metallographic preparation, consisting of silicon carbide paper grinding and diamond suspension polishing, a final polishing step with colloidal silica was applied.

Compressive tests were conducted at 25 °C by means of an MTS 2/M machine, equipped with extensometer, at strain rate of 0.01 min^{-1}. Eight complete loading and unloading cycles, up to 10% in maximum strain, were carried out on specimens in as-built condition and after a low-temperature heat treatment, for stress release and shape setting, at 500 °C for 5 min followed by water quench.

Results and Discussion

Processability of NiTi Powder Using SLM

A feasible processing window was identified by considering the main process parameters, including laser power and exposure time (see Table 1), which determine the energy transferred by the laser beam to the powder layer during the PW emission mode.

In detail, in the present work, the processability was correlated to the maximization of the relative density, the latter was measured via the Archimede's method. Figure 1 shows the effect of the fluence F, which is directly proportional to the pulse energy (product between laser power and exposure time), on the densification of the NiTi powder. The curve, depicted in Fig. 1, represents the typical evolution of the relative density as function of F for SLMed parts, which can be found in the literature for several alloys. A rapid increase of the relative density up to its maximum value can be observed, then a stable part follows and finally density decays smoothly for higher values of F (see the red dashed lines (1), (2) and (3) in Fig. 1, respectively. In the case of the NiTi alloy, a steep increase in the relative density up to 99.7% was detected with increasing values of F up to 63 J/mm^3, which corresponds to the process condition, defined by P = 30 W and t_{exp} = 120 µs (see the red circle on the left in Fig. 2). For limited increase of the laser energies, the relative density remained slightly constant up to F equal to 160 J/mm^3 (process condition, defined by P = 125 W and t_{exp} = 75 µs; see the red circle on the right in Fig. 2), which corresponds to a relative density value of 99.9%. Finally, for further increase of energy, the relative density started to

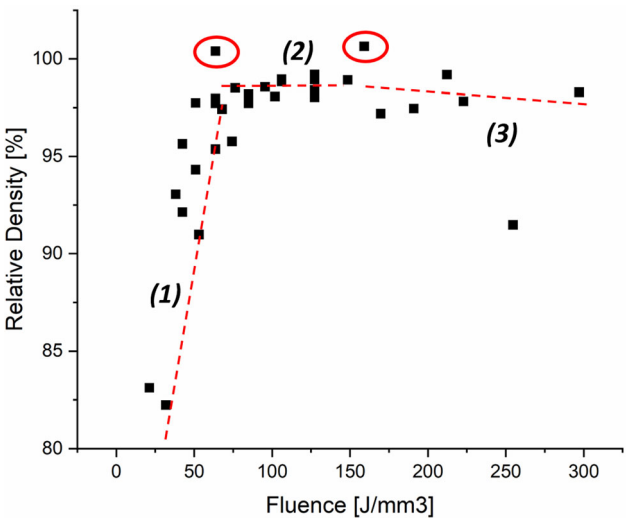

Fig. 1 Relative density of NiTi samples in function of the fluence F

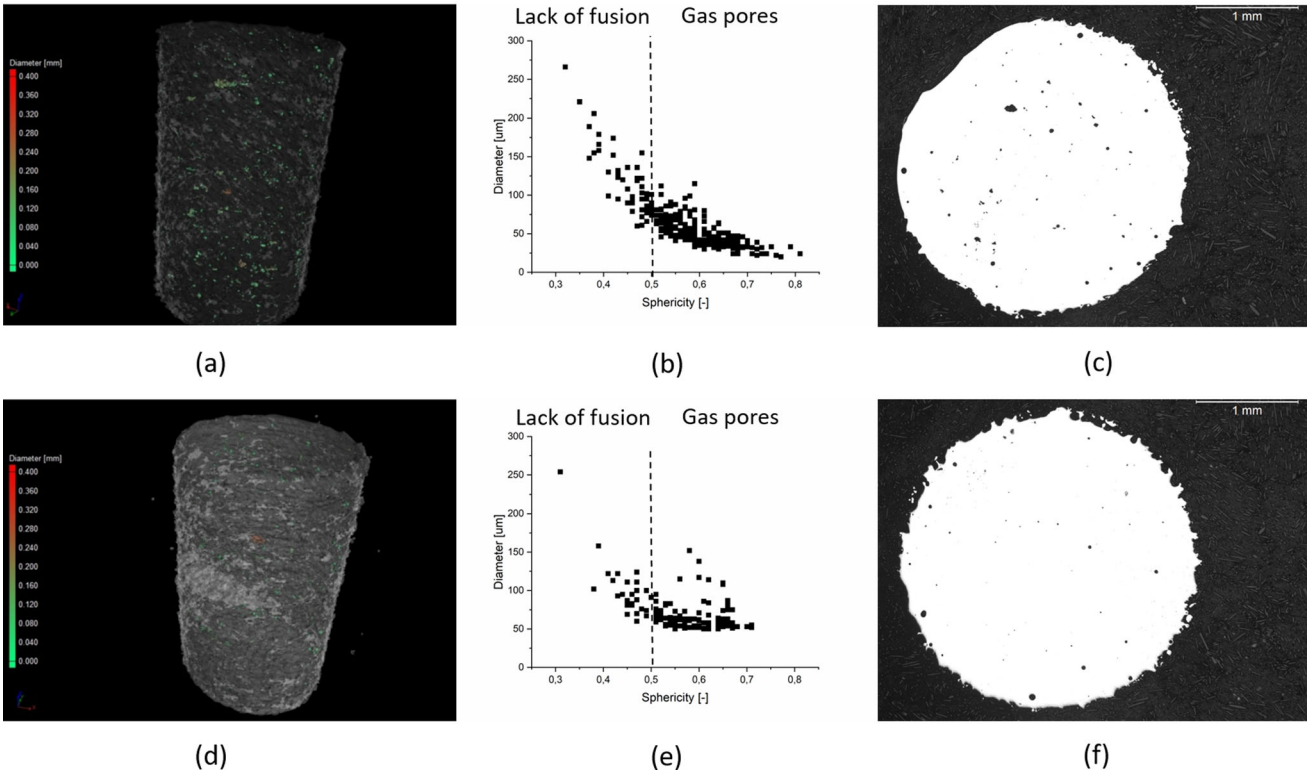

Fig. 2 Analysis of defects, by CT and OM, respectively, of NiTi samples manufactured with different energy density values: F = 63 J/mm^3 (a-b-c) and F = 160 J/mm^3 (b-d-f). In the Fig. 3D, CT scans (**a**, **d**), diameter-sphericity trend (**b**, **e**), and cross section in the xy view (**c**, **f**)

slowly decrease, since higher fluence can induce the formation of gas pores.

It is known that this particular trend can usually be explained by considering that the adoption of low-energy inputs causes defects, such as unmelted powders, due to the lack of fusion. On the contrary, high-energy ones induce porosity, due to gas entrapment and potential local vaporization of elements. The mentioned different kinds of defects are located in the regions (1) and (3) in the relative density evolution shown in Fig. 2. In particular, the presence of these different defects can be explained by the energy required by the material to allow its melting and its partial vaporization, according to the following equation (Eq. 2):

$$E = A \cdot \rho \cdot \left\{ C_p \cdot [T_M - T_i] + L_M + m' \cdot L_V \right\} \quad (2)$$

where A is the absorption coefficient; r is the density; Cp is the thermal capacity; T_M and T_i are the melting and initial temperatures, respectively; L_M and L_V are the latent heat of melting and vaporization, respectively; and m′ represents the percentage of liquid material that is subjected to vaporization, if present.

Combining Eqs. 1 and 2, it can be obtained that the density of energy per unit of volume, transferred by the laser beam to the powder and representative of the specific process condition, is correlated to the energy required by the alloy for its melting and, eventually, for its partial evaporation (if $m' > 0$). For typical defects of SLMed parts, such as lack of fusion or gas pores, the fluence F would be lower or higher than E, respectively.

In Fig. 2, CT scans and optical micrographs of sections were combined in order to analyze the defects in NiTi-built cylinders, produced with the extreme conditions of the region (2) of Fig. 1. In details, Fig. 3a, d report 3D reconstructions of the large volume samples from CT scans, while the correlations between the defect diameter and its sphericity are plotted in Fig. 3 b, e. Additionally, OM was adopted for analyzing the cross section (xy view) of the samples.

It can be seen that the NiTi sample, produced with fluence equal to 63 J/mm^3 (P = 30 W; t_{exp} = 125 µs), shows residual porosity (residual porosity = 100%—relative density), which is in good agreement with the relative density value measured with Archimede's method (see Fig. 1). These defects are spread all across the sample volume without any preferential location, as shown in Fig. 3a. Figure 3b indicates that the detected pores size varied from 30 µm up to 270 µm, and the corresponding sphericity factor ranged from 0.82 down to 0.34, respectively. The cross section of Fig. 2c exhibits a representative distribution of the size, shape, and position of the defects;

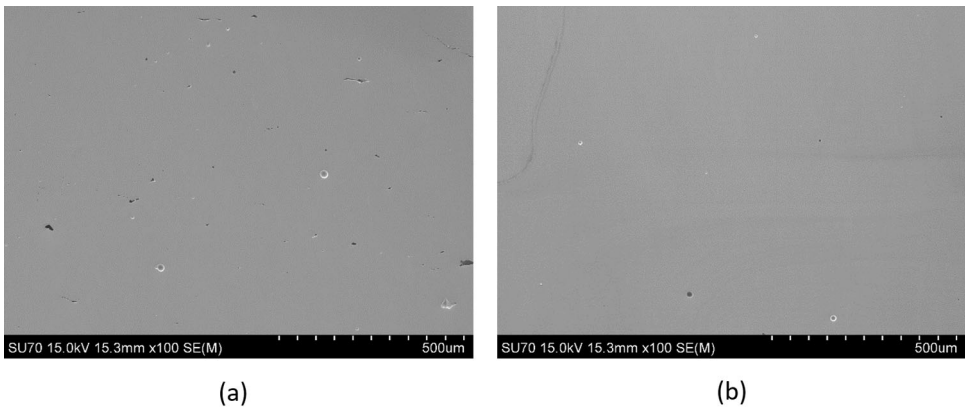

Fig. 3 SEM micrographs in the xz view of the NiTi samples manufactured with different energy density values: F = 63 J/mm^3 (**a**) and F = 160 J/mm^3 (**b**); building direction vertical

in fact, the large variation in the defects size can be well appreciated by the OM image.

The increase of fluence to 160 J/mm^3 (P = 125 W; t_{exp} = 75 μs) leads to lowering the residual porosity down to 0.1%, evenly distributed in the entire volume of the built sample, as shown in Fig. 2d. The number of detected defects and their size and shape is lower than in the previous sample, as indicated in Fig. 2e: the pores size varied from 60 μm up to 125 μm, except for few outliers, and their corresponding sphericity factor ranged from 0.72 down to 0.43, respectively. The observation of the cross section acquired with OM confirms that the level of porosity has been reduced (see Fig. 2f). The enhancement in terms of relative density as well as the reduction of the defects size is due to the increase of the energy transferred to the powder bed, which provokes a larger liquid pool and better joining between adjacent pools.

Both the plots reported in Fig. 3b and e are divided into two regions: lack of fusion in correspondence of irregular and large size defects, and gas pores, characterized by smaller dimension and high sphericity. SEM analysis confirmed the different types of porosity that could be found in the samples (see Fig. 3): while the lower fluence sample presented both round pores from gas trapping and irregular pores from lack of fusion, higher fluence sample mostly presented mostly round pores.

These regions can be correlated to the process conditions and mainly to the fluence. The first region can be correlated to insufficient energy for the complete melting of the powder; therefore, elongated and irregular voids are generated along a preferential direction, related to the laser scanning. With increasing energy density, the second region is characterized by finer and spherical porosities: higher energy given to the powder can promote the formation of a more uniform and stable liquid pool, which allows for an increase in the relative density of the SLMed part [35].

Representative 3D profiles of the surfaces of NiTi samples obtained at F = 63 and 160 J/mm^3 are shown in Fig. 4 and surface parameters are reported in Table 2: the good achieved densification is confirmed at the surface level too. Surface roughness expressed as Sa (Arithmetical mean height of the surface) or Sq (Root mean square height of the surface) were comparable for both the type of samples at any surface scale and whatever the acquisition technique. As these parameters involve the distribution of heights along the examined surfaces, they do not account for the spatial distribution of the surface features; however, a different pattern regularity can be observed on the surfaces of NiTi samples obtained at different energy densities. A useful spatial parameter able to quantitatively determine this feature is the Str (Texture Aspect Ratio) which can assume values ranging from 0, for surfaces exhibiting regular directionality and privileged orientations, to 1 for surfaces having an isotropic random texture [36]. The values of Str presented in Table 2 are lower for the surface of NiTi samples obtained at F = 160 J/mm^3 demonstrating a more regular surface pattern compared to samples obtained at F = 63 J/mm^3. This confirms that higher fluence value permits to achieve a complete melting of the NiTi powder, and the smoother upper surface indicates that a higher densification can also be obtained, as indicated in the previous analysis of the defects. However, as expected, the presence of partial melted residual powder was also visible from both the 3D images, acquired at high magnification (see Fig. 4b, d).

Martensitic Transformation, Microstructure, and Mechanical Behavior

In Fig. 5, the DSC curves of small NiTi samples, produced with the different values of fluence and the reference DSC scan of starting powder, are depicted. Both forward and back transformation peaks of as-built SLMed are broad with low enthalpy values due to high residual stresses as consequence of the rapid solidification of SLM layer-by-layer process. Again, upon cooling typical double steps transformation B2-R-B19′ is shown,

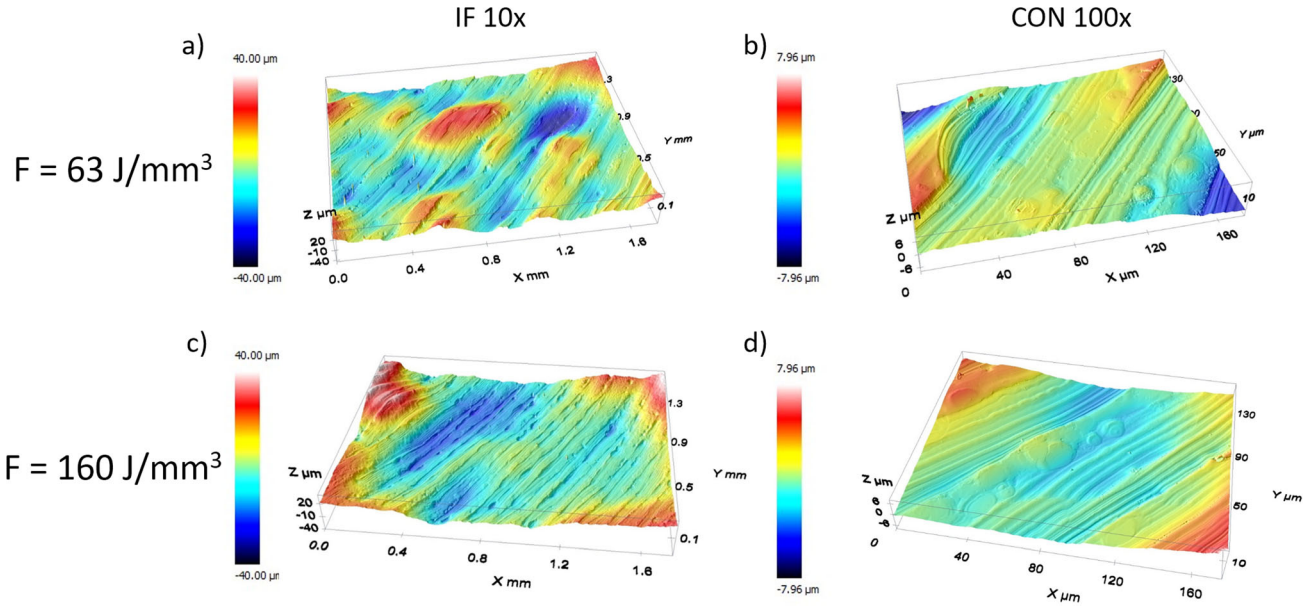

Fig. 4 3D reconstruction of surface scans of NiTi samples manufactured with different energy density values: F = 63 J/mm^3 (**a**, **b**) and F = 160 J/mm^3 (**c**, **d**)

Table 2 Surface parameters obtained by interferometric and confocal microscopy for NiTi samples obtained at different fluence values

Fluence, F [J/mm^3]	10 × interferometric (1.75 × 1.32 mm^2)			100 × confocal (175 × 132 µm^2)		
	Sa [µm]	Sq [µm]	Str	Sa [µm]	Sq [µm]	Str
63 J/mm^3	8.66	11.07	0.69	1.26	1.68	0.72
160 J/mm^3	8.08	11.52	0.48	1.25	1.59	0.46

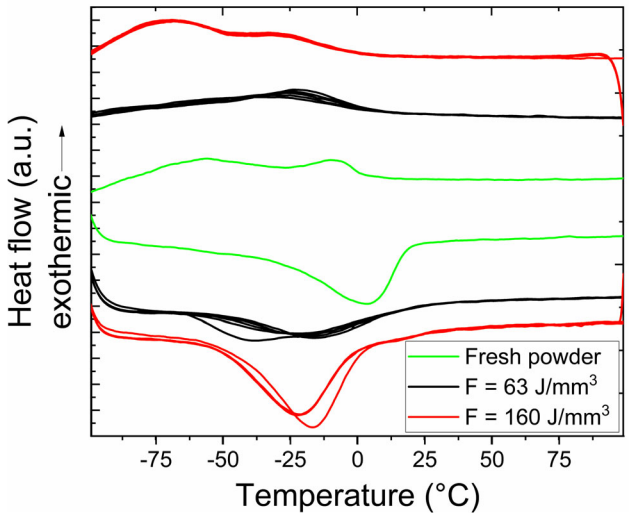

Fig. 5 DSC scans of NiTi samples manufactured with different energy density values: F = 63 J/mm^3, F = 160 J/mm^3, and reference powder

while for the high residual stresses condition, only a broad peak related to reverse martensite to austenite (B2) is highlighted.[37, 38].

EDXS analyses were performed on the cross section of the two samples, and no evident compositional variations were detected (see Table 4). Anyways, it is worth mentioning that the increase of fluence is correlated to a slight decrease of the average Ni content from 51.0 down to 50.8 in atomic percentage; thus, it should be correlated to the temperatures shift, as those are very sensible to Ni/Ti ratio [38].

As expected, after HT, the DSC curves, depicted in Fig. 6, show a marked double-step transformation for both the heating and the cooling scans. A slight increasing of R-M peak for higher value of fluence can be associated to a very slight increasing of Ni content as reported above. Because R phase is less affected by the Ni/Ti ratio, the peaks associated to R phase transformation are basically overlapping. Details of MT temperatures and enthalpies of SLM samples after HT are collected in Table 3.

The shift of the MT temperatures can be due to several reasons, such as Ni loss, residual stresses, and microstructural modifications. EDXS analyses were performed on the cross section of the two samples, and no evident compositional variations were detected (see Table 4). Anyways, it is worth mentioning that the increase

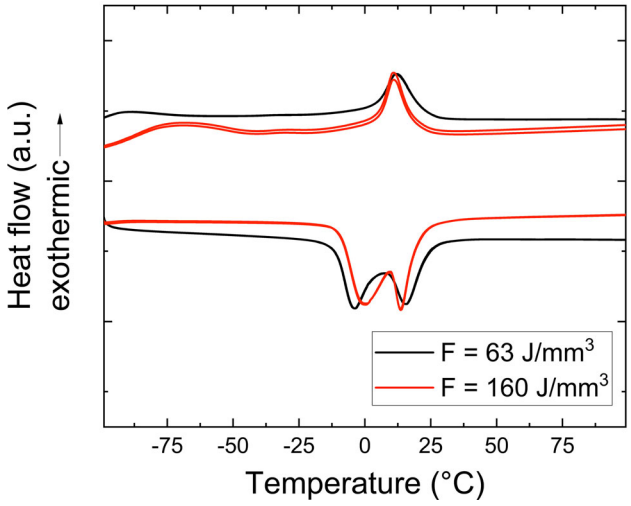

Fig. 6 DSC scans of NiTi samples manufactured with different energy density values: F = 63 J/mm^3 and F = 160 J/mm^3 after HT at 500 °C for 10 min + WQ

of fluence is correlated to a slight decrease of the average Ni content from 51.0 down to 50.8 in atomic percentage: this should be correlated to the transformation temperatures shift, as those are very sensible to Ni/Ti ratio [38]. This trend is confirmed for a very high-fluence value (300 J/mm^3) SLM specimen where a Ni composition of 50.4 at.% was detected (see Table 4). However, very poor density samples with fluence values higher than 160 were not considered in this work.

Microstructural investigations were performed on the two selected samples. For both samples, grains shape was irregular on XY section and characterized by a rather squared patter, with bigger grain at center surrounded by smaller ones. On XZ section, grains appeared elongated, as generally shown by SLMed materials. Significant differences were detected with EBSD analyses, and those main results are presented in Figs. 7, 8, and 9. Low fluence sample shows random orientation of the grains, while in the high-fluence sample, the grains show a preferred [100] orientation rather parallel to z direction (building direction). The found preferred orientation agrees with literature results [30, 39, 40]. This difference in orientation is quite evident in Fig. 7, in which analyses performed on xy section are reported. OIM and pole figures, related to orientation with respect to building direction, clearly denote the

Table 4 EDS analysis of the NiTi-built samples manufactured with different energy density values

Fluence, F [J/mm3]	Ti [at%]	Ni [at%]
63 J/mm^3	49.0 ± 0.3	51.0 ± 0.3
160 J/mm^3	49.2 ± 0.3	50.8 ± 0.3
300 J/mm^3	49.6 ± 0.3	50.4 ± 0.2

difference between the two conditions. Additionally, in Fig. 7a, the regular pattern due to the parallel scanning lines can also be observed, separated of 50 µm, i.e., the hatch distance.

Analyses performed on xz section (see Fig. 8) confirmed the different preferred orientation with respect to xy ones and also highlighted a sharper epitaxial growth in the high-fluence sample. Figure 8d shows elongated grains that nucleates in a melt pool and continued through several building layers.

Both microstructural features, namely, preferred orientation and elongated grains, are known to affect shape memory materials properties [19]. Higher-magnification analyses allowed to verify the presence of both bigger grains, and also micrometric size ones, often clustered, with similar orientation (see Fig. 9). Grain boundaries appear wavy, denoting a far from equilibrium configuration of the microstructure and high energy stored in grain boundaries, that can be released upon thermal treatment.

Figure 10a, b display loading/unloading curves of samples, produced with fluence equal to 63 and 160 J/mm^3, respectively. The trend of recovered strain vs imposed deformation is shown in Fig. 10c. During initial cycles, the two samples display a qualitatively similar behavior: recovered strains increase almost linearly at every cycle, but at lower fluence higher superelasticity can be obtained. Moreover, it is characterized by higher stresses (e.g., 300 MPa vs. 151 MPa at 3% deformation). When imposed strain exceeds 6%, however, the superiority of the sample processed with the low fluence value in recovering strain is reversed and the increase of fluence provokes a better behavior [30]. In particular, whereas the use of low fluence permits to achieve the ability to recover deformation like a plateau, certainly due to the accumulation of irreversible

Table 3 Transformation temperatures peaks and heat exchange, evaluated at the second thermal cycle, of the NiTi-built samples after HT 500 °C for 10 min + wq

Conditions	$P_{A\rightarrow R}$ [°C]	$P_{R\rightarrow M}$ [°C]	$P_{M\rightarrow R}$ [°C]	$P_{R\rightarrow A}$ [°C]	$H_{M\rightarrow A}$ [J/g]
F = 63 J/mm^3	12	− 89	− 4.4	15.0	13
F = 160 J/mm^3	11	− 72	− 0.5	15.0	15.9

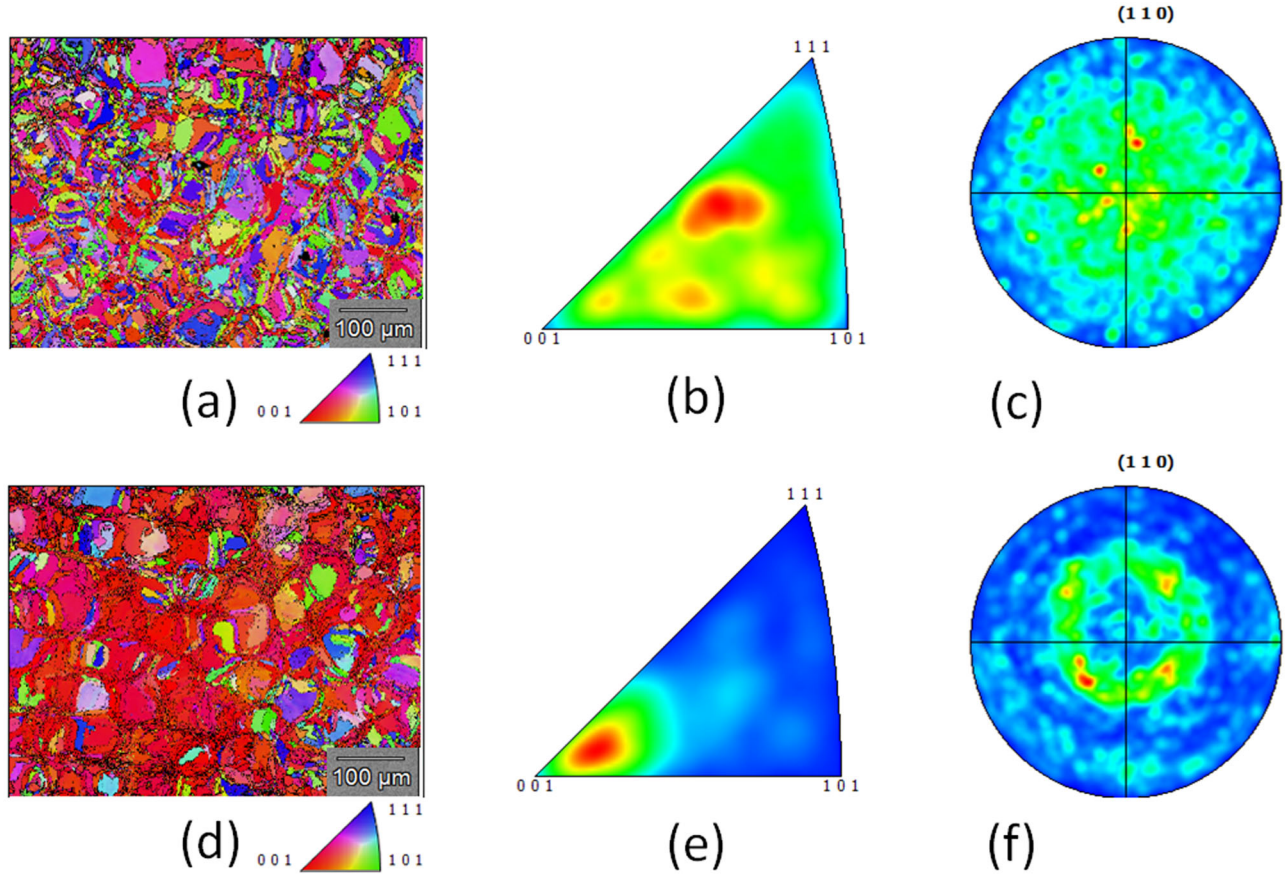

Fig. 7 Results of EBSD analyses performed on the xy section of NiTi samples manufactured with F = 63 J/mm^3 (a-b-c) and F = 160 J/mm^3 (d-e-f). OIM (**a**, **d**) and IPF (**b**, **e**) according to Building Direction (normal to the section), (110) Pole Figures (**c**, **f**)

plastic deformation, the recovered deformation by using higher fluence keeps increasing linearly.

Effect of Low-Temperature Heat Treatment on Functional Properties

A loading/unloading test was also performed on the sample produced with low- and high-fluence values after heat treatment, as shown in Fig. 11. It may be appreciated that the mechanical response changed, giving rise to the well-known flag-like behavior, with evident formation of reversible stress-induced martensite plateau, with loading/unloading mechanical hysteresis of about 200 MPa at 3% in strain and a complete compressive superelastic effect, with recovery strain of 6% at room temperature. For higher fluence, a reduction of the stress values can be correlated to major texture in [100] direction that it would create a larger bias than other orientation and the transformation is favored [41].

Conclusions

Selective Laser Melting confirmed to be a suitable AM technology for producing NiTi. The process parameters need to be properly adjusted to reach high-density material:

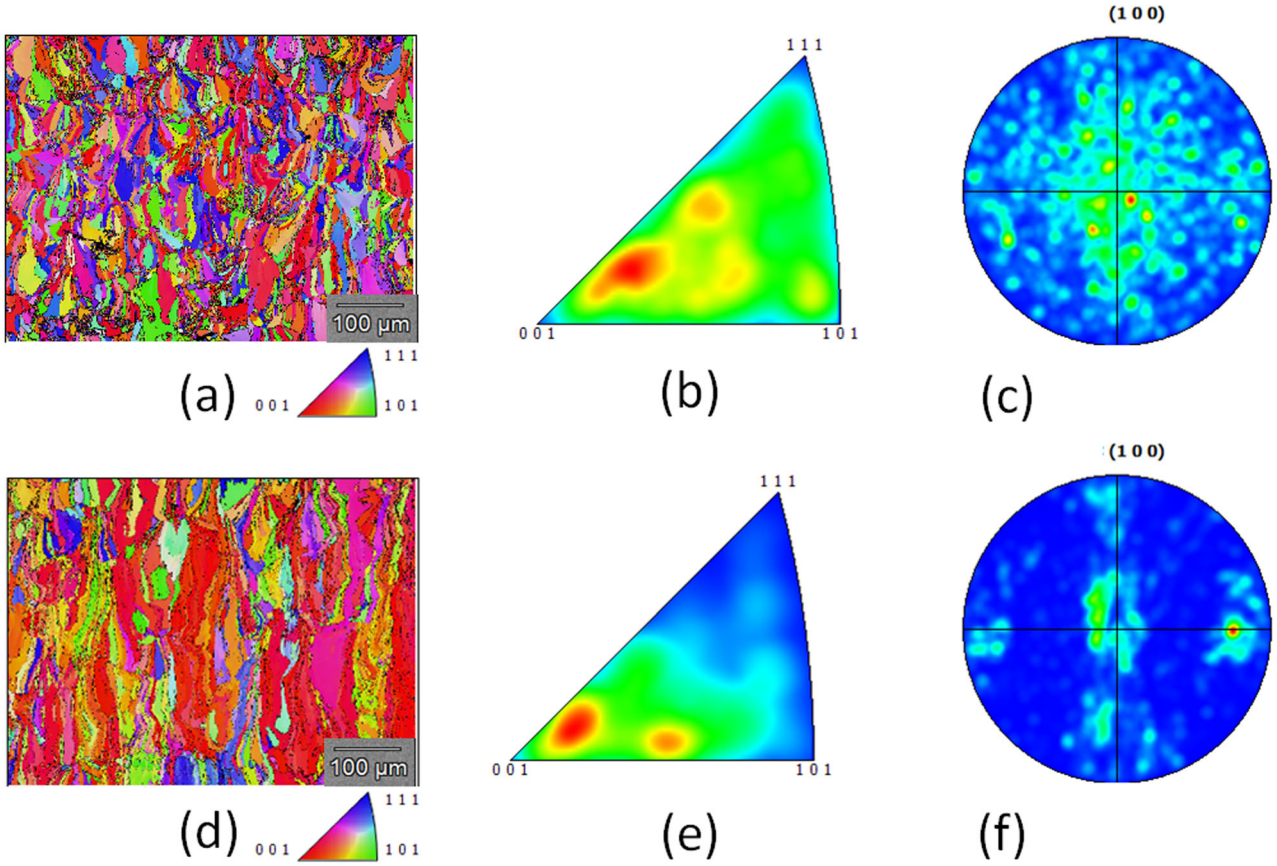

Fig. 8 Results of EBSD analyses performed on the xz section of NiTi samples manufactured with F = 63 J/mm^3 (a-b-c) and F = 160 J/mm^3 (d-e-f). OIM (**a**, **d**) and IPF (**b**, **e**) according to Building Direction (vertical in the section), (100) Pole Figures (**c**, **f**)

it was found that for laser fluence of about 160 W/mm^3 a density of 99.9% is reached.

Porosity of the material is strongly affected by laser fluence and for each AMed part a compromise between the irregular defects due to lack of fusion and the gas entrapment spherical pore needs to be reached. Anyways, homogeneous distribution of defects was found in the entire volume of the SLMed parts. The upper surface morphology, correlated to the roughness of the part, can be modified by changing the fluence. A limited Ni evaporation, proportional to the laser fluence, was indirectly observed with DSC analysis, correlated to EDS measurements. Depending on the selected process parameters, SLMed NiTi can show a (100) preferred out of plane orientation along the building direction, while on xz section, the grains exhibit a partial epitaxial grown. The SLMed parts, in as-built condition, are characterized by a rapid solidification microstructure suitable for promoting a complete superelasticity that can be triggered by a low-temperature annealing.

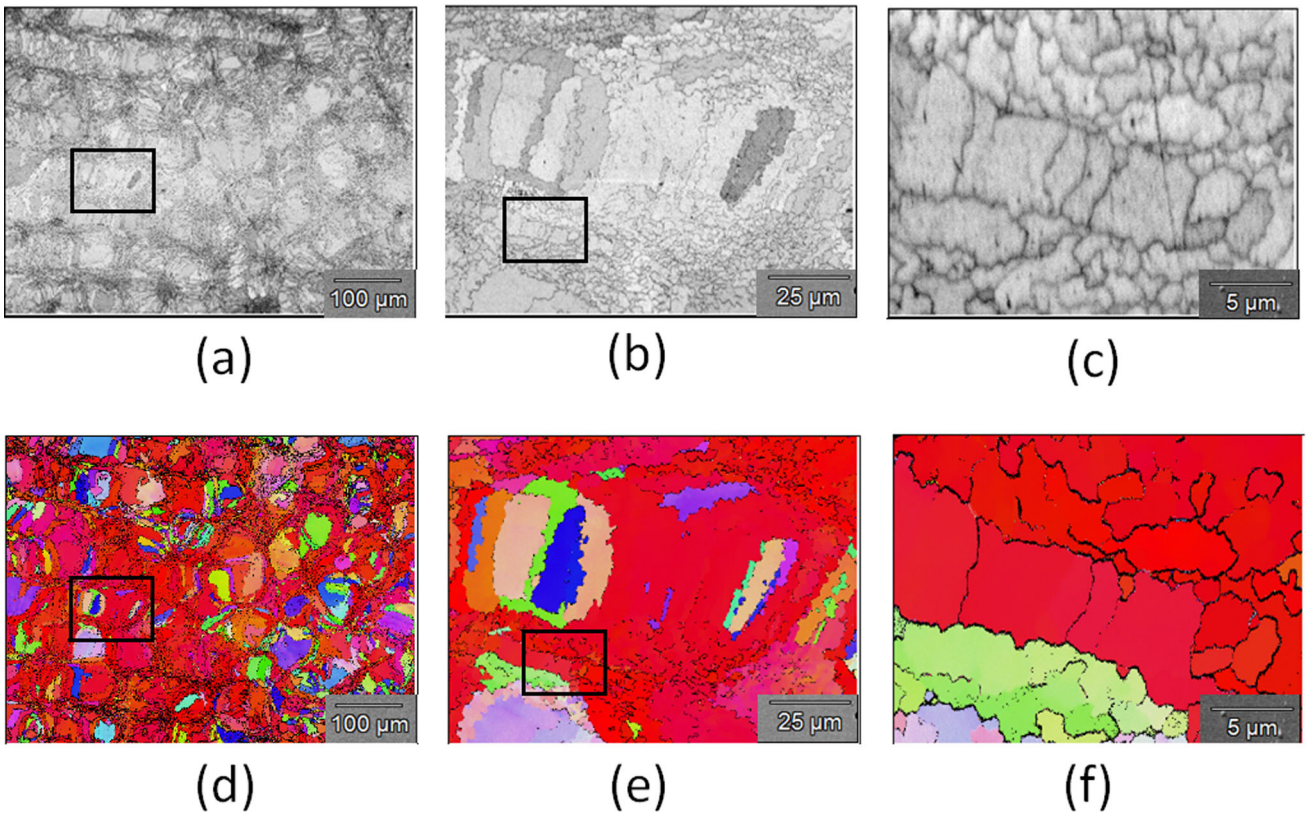

Fig. 9 EBSD analyses, carried out at increasing magnifications, on the xy surface of the NiTi sample produced with F = 160 J/mm^3 (**a**, **b**, **c**): pattern quality maps, (**d**, **e**, **f**) OIM according to building direction. **b–e** and **c–f**: highe- magnification analyses of the areas in black boxes on figures **a–d** and **b–e,** respectively

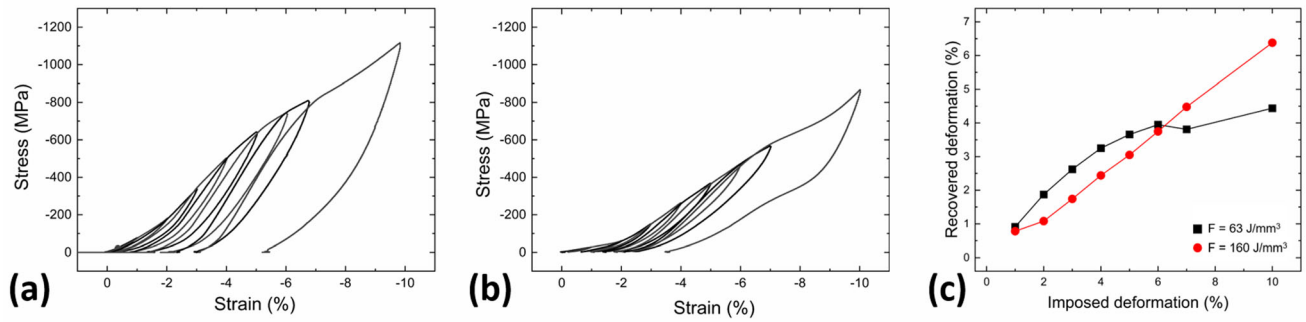

Fig. 10 Compressive response during cycling of NiTi as-built samples manufactured with different energy density values: F = 63 J/mm^3 (**a**); F = 160 J/mm^3 (**b**); and recoverable strain (**c**)

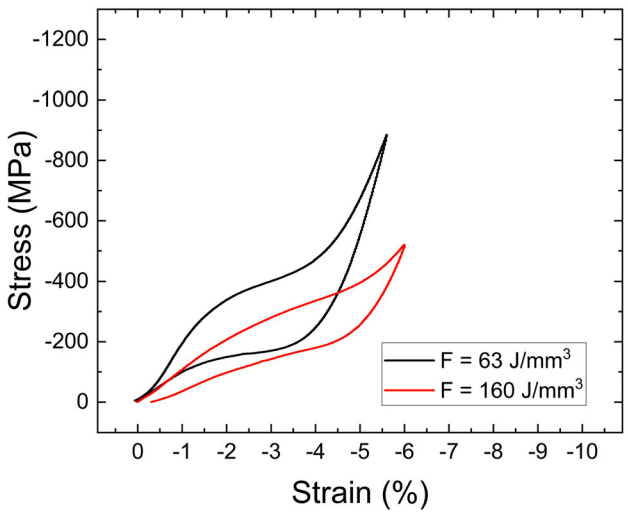

Fig. 11 Compressive response of the NiTi samples, subjected to heat treated at 500 °C

Acknowledgements The authors would like to acknowledge Saes Getters SpA as supplier of Nitinol powder. The authors would like to thank Nicola Bennato from CNR ICMATE for his support in the experimental activity.

References

1. Funakubo H (1987) Shape memory alloys. Gordon and Breach Science Publishers, Amsterdam
2. Casati R, Vedani M, Tuissi A (2014) Thermal cycling of stress-induced martensite for high-performance shape memory effect. Scr Mater 80:13–16
3. Nishida M, Wayman C, Honma T (1986) Precipitation processes in near-equiatomic TiNi shape memory alloys. Metall Mater Trans 17:1505–1515
4. Elahinia M, Hashemi M, Tabesh M, Bhaduri SB (2012) Manufacturing and processing of NiTi implants: a review. Prog Mater Sci 57:911–946
5. Weinert K, Petzoldt V (2004) Machining of NiTi based shape memory alloys. Mater Sci Eng A 378:180–184
6. Donohue B (2009) Developing a good memory—nitinol shape memory alloy, Today's Machining World 42–48
7. Manjaiah M, Narendranath S, Basavarajappa S (2014) Review on non-conventional machining of shape memory alloys. Trans Nonferrous Met Soc 24:12–21
8. Bharathi Kannan TD, Ramesh T, Sathiya P (2016) A Review of similar and dissimilar micro-joining of nitinol. JOM 68:1227–1245
9. Oliveira JP, Miranda RM, Braz Fernandes FM (2017) Welding and joining of NiTi shape memory alloys: a review. Prog Mater Si 88:412–466
10. Falvo A, Forgiuele FM, Maletta C (2005) Laser welding of a NiTi alloy: mechanical and shape memory alloy. Mater Sci Eng A 412:235–240
11. Biffi CA, Tuissi A (2017) Nitinol laser cutting: microstructure and functional properties of femtosecond and continuous wave laser processing. Smart Mater Struct 26:035006
12. Tuissi A, Besseghini S, Ranucci T, Squatrito F, Pozzi M (1999) Effect of Nd-YAG laser welding on the functional properties of the Ni–49.6 at.%Ti. Mater Sci Eng A 273–275:813–817
13. Elahinia M, Shayesteh Moghaddam N, Taheri Andani M, Amerinatanzi A, Bimber BA, Hamilton RF (2016) Fabrication of NiTi through additive manufacturing—a review. Prog Mater Sci 83:630–663
14. Van Humbeeck J (2018) Additive manufacturing of shape memory alloys. Shape Mem Superelasticity 4–2:309–312
15. Biffi CA, Tuissi A (2017) Stato dell'arte sulle tecniche di produzione additiva per metalli. Metall Ital 1:5–10
16. Mitchell A, Lafont U, Hołyńska U, Semprimoschnig U (2018) Additive manufacturing—a review of 4D printing and future applications. Addit Manuf 24:606–626
17. Bormann T, Schumacher R, Müller B, Mertmann M, De Wild M (2012) Tailoring selective laser melting process parameters for NiTi implants. J Mater Eng Perform 21:2519–2524
18. Saedi S, Turabi AS, Andani MT, Haberland C, Karaca H, Elahinia M (2016) The influence of heat treatment on the thermomechanical response of Ni-rich NiTi alloys manufactured by selective laser melting. J Alloys Compd 677:204–210
19. Shayesteh Moghaddam N, Saedi S, Amerinatanzi A, Hinojos A, Ramazani A, Kundin J, Mills MJ, Karaca H, Elahinia M (2019) Achieving superelasticity in additively manufactured NiTi in compression without post-process heat treatment. Sci Rep 9:41
20. Zhou Q, Dilawer Hayat M, Chen G, Cai S, Qu X, Tang H, Cao P (2019) Selective electron beam melting of NiTi: microstructure, phase transformation and mechanical properties. Mater Sci Eng A 744:290–298
21. Hamilton RF, Bimber BA, Palmer TA (2018) Correlating microstructure and superelasticity of directed energy deposition additive manufactured Ni-rich NiTi alloys. J Alloys Compd 739:712–722
22. Wang C, Tan XP, Du Z, Chandra S, Sun Z, Lim CWJ, Tor SB, Lim CS, Wong CH (2019) Additive manufacturing of NiTi shape memory alloys using pre-mixed powders. J Mater Process Technol 271:152–161
23. Saedi S, Moghaddam NS, Amerinatanzi A, Elahinia M, Karaca HE (2018) On the effects of selective laser melting process parameters on microstructure and thermomechanical response of Ni-rich NiTi. Acta Mater 14:552–560
24. Speirs M, Wang X, Van Baelen S et al (2016) On the Transformation behavior of NiTi shape-memory alloy produced by SLM. Shape Mem Superelasticity 2:310–316
25. Shiva S, Palani IA, Mishra SK, Paul CP, Kukreja LM (2015) Investigation on the influence of composition in the development of Ni-Ti shape memory alloy using laser based additive manufacturing. Opt Laser Technol 69:44–51
26. Mahmoudi M, Tapia G, Franco B, Ma J, Arroyave R, Karaman I, Elwany A (2018) On the printability and transformation behavior of nickel-titanium shape memory alloys fabricated using laser powder-bed fusion additive manufacturing. J Manuf Process 35:672–680
27. Bormann T, Muller B, Schinhammer M, Kessler A, Thalmann P, de Wild M (2014) Microstructure of selective laser melted nickel-titanium. Mater Charact 94:189–202
28. Andani MT, Saedi S, Turabi AS, Karamooz MR, Haberland C, Karaca HE, Elahinia M (2017) Mechanical and shape memory properties of porous $Ni_{50.1}Ti_{49.9}$ alloys manufactured by selective laser melting. J Mech Behav Biomed Mater 68:224–231
29. Moghaddam NS, Saghaian SE, Amerinatanzi A, Ibrahim H, Li P, Toker GP, Elahinia M (2018) Anisotropic tensile and actuation properties of NiTi fabricated with selective laser melting. Mater Sci Eng A 724:220–230
30. Dadbakhsh S, Vrancken B, Kruth JP, Luyten J, Van Humbeeck J (2016) Texture and anisotropy in selective laser melting of NiTi alloy. Mater Sci Eng A 650:225–232
31. Biffi CA, Fiocchi J, Bassani P, Tuissi A, Microstructure and martensitic transformation of selective laser melted NiTi shape

memory alloy parts, proceedings of the second international conference on simulation for additive manufacturing (Sim-AM 2019, Pavia, Italy, 11–13 September 2019. ISBN: 978-84-949194-8-0.
32. Assuncao E, Williams V (2013) Comparison of continuos wave and pulsed wave laser welding effects. Opt Lasers Eng 51:674–680
33. Demir AG, Colombo P, Previtali B (2017) From pulsed to continuous wave emission in SLM with contemporary fiber laser sources: effect of temporal and spatial pulse overlap in part quality. Int J Adv Manuf Technol. https://doi.org/10.1007/s00170-016-9948-7
34. Biffi CA, Fiocchi J, Bassani P, Tuissi A (2018) Continuous wave vs pulsed wave laser emission in selective laser melting of AlSi10Mg parts with industrial optimized process parameters: microstructure and mechanical behaviour. Add Manuf 24:639–646
35. Fiocchi J, Biffi CA, Tuissi A (2019) Selective laser melting of high-strength primary AlSi9Cu3 alloy: processability, microstructure, and mechanical properties. Mater Des 191:108581
36. Leach R (2013) Characterisation of areal surface texture. Springer-Verlag, Berlin Heidelberg
37. Khalil Allafi J, Ren X, Eggeler G (2002) The mechanism of multistage martensitic transformations in aged Ni-rich NiTi shape memory alloys. Acta Mater 50(4):793–803
38. Dadbakhsh S, Speirs M, Kruth J-P, Schrooten J, Luyten J, Van Humbeeck J (2014) Effect of SLM parameters on transformation temperatures of shape memory nickel titanium parts. Adv Eng Mater 16:1140–1146
39. Biffi CA, Bassani P, Nematollahi M, Moghaddam NS, Amerinatanzi A, Mahtabi MJ, Elahinia M, Tuissi A (2019) Effect of ultrasonic nanocrystal surface modification on the microstructure and martensitic transformation of selective laser melted nitinol. Materials 12(19):3068
40. Biffi CA, Bassani P, Fiocchi J, Tuissi A (2020) Microstructural and mechanical response of NiTi lattice 3D structure produced by selective laser melting. Metals 10:814. https://doi.org/10.3390/met10060814
41. Gall K, Sehitoglu H (1999) Therole of texture in tension-compression asymmetry in policrystalline NiTi. Int J Plast 15:69–92